Wireless Communication in Modular Multilevel Converters and Electromagnetic Interference Characterization

Ciftci, Baris; Gross, James; Augustin, Tim; Wang, Xiongfei; Norrga, Staffan; Nee, Hans Peter

Published in:
IEEE Access

DOI (link to publication from Publisher):
10.1109/ACCESS.2022.3165206

Publication date:
2022

Document Version
Publisher's PDF, also known as Version of record

IEEE Access
Multidisciplinary ⋮ Rapid Review ⋮ Open Access Journal

Received January 25, 2022, accepted March 20, 2022, date of publication April 6, 2022, date of current version April 14, 2022.

Digital Object Identifier 10.1109/ACCESS.2022.3165206

Wireless Communication in Modular Multilevel Converters and Electromagnetic Interference Characterization

BARIŞ ÇIFTÇI, (Graduate Student Member, IEEE), JAMES GROSS, (Senior Member, IEEE), TIM AUGUSTIN, XIONGFEI WANG, (Senior Member, IEEE), STAFFAN NORRGA, (Member, IEEE), AND HANS-PETER NEE, (Fellow, IEEE)
KTH Royal Institute of Technology, 100 44 Stockholm, Sweden

Corresponding author: Barış Çiftçi (bacif@kth.se)

ABSTRACT The wireless control of modular multilevel converter (MMC) submodules was recently proposed. The success of the control depends on specialized control methods suitable for wireless communication and a properly designed wireless communication network in the MMC valve hall while aiming for low latency and high reliability. The wireless communication in the hall can be affected by the electromagnetic interference (EMI) of MMC submodules, voltage and current transients. In this article, firstly, a wireless communication network based on 5G New Radio is designed for an example full-scale MMC valve hall. After that, the radiated EMI characteristics of the MMC submodules with different voltage and current ratings and two dc circuit breakers are measured. The effects of EMI on wireless communication in the multi-GHz frequency band are tested. The interference from the components is confined below 500 MHz, and the wireless communication with 5825 MHz center frequency is not affected by the interference.

INDEX TERMS 5G mobile communication, circuit breakers, electromagnetic interference, multilevel converters, wireless communication.

I. INTRODUCTION

The modular multilevel converter (MMC) is extensively used in high-voltage multi-megawatt applications such as high-voltage dc (HVdc) transmission systems [1]. The communication between the MMC central controller and the submodules is commonly realized by optical fiber cables as they are reliable, immune to electromagnetic interference (EMI), and provide galvanic isolation between the connecting entities [2]. On the other hand, the total number of MMC submodules to reach the targeted power ratings might be in the range of thousands [3], and the dimensions of MMC valve halls might rise to hundreds of meters [4] for HVdc transmission applications. Therefore, substantial issues arise from cable-based deployment of large MMC valve halls:

1) Laying out, terminating, and insulation-testing thousands of fiber cables with hundreds of meters in length requires a significant workforce and time during the installation of the MMC. Moreover, each cable needs to be identified and checked whether it connects the correct terminals during the commissioning of the MMC, which further increases the required workforce and time [5]. The required resources for all these processes contribute to the initial cost of the MMC station, with several other factors mostly specific to the project. Furthermore, in case of a delay in the commissioning of the MMC, significant fines might be incurred to the MMC contractor, which might correspond to or even exceed the profit margin. Examples of voltage-sourced converter overall costs in HVdc transmission applications, which are considered to be mainly MMCs, are available in the literature: The cost of a converter station per MW ranges from 218 €k/MW to 429 €k/MW in [6] for eight different projects with power ratings from 700 MW to 3000 MW. Cigre exemplifies the converter cost as 102 €k/MW and 220 €k/MW for two projects with 1500 MW and 1000 MW ratings [7]. The share of fiber-cable-related costs in the overall costs of an MMC station is not publicly available to the authors' best knowledge. On the other hand, typical commissioning and erection costs for a new HVdc facility are estimated

The associate editor coordinating the review of this manuscript and approving it for publication was Tariq Masood.

as 8 % of the overall costs in [8], while the exact cost structure is unclear.

2) The routing of the thick cable bundles in the MMC valve hall can be cumbersome and requires a resource-intensive mechanical design process. Further, the bundles might complicate the replacement of the (failed) submodules during the maintenance of the MMC, thus increasing the maintenance time.
3) With thousands of submodules and hundreds of meter valve hall dimensions, the total length of optical fiber cables in an MMC valve hall is possibly in the range of hundreds of kilometers. This much of cables lead to an increase in the converter footprint, weight, and volume, which are problematic, especially in off-shore and in-city transmission platforms [9].
4) Although the insulation of the fiber cables is tested during the installation, the cables present an insulation breakdown risk between the central controller (low-voltage area) and the submodules (high-voltage area) due to, e.g., accumulation of dust and humidity on them over time. In order to minimize the risk, proper air conditioning and filtration are required in the valve hall, which might increase the costs.
5) The fiber cables risk spreading fire in the MMC valve hall [10]. To minimize the risks, cables made from special material and with coatings are to be used, such as flame-retardant, non-combustible, or self-extinguishing, which increase the cost and might complicate the layout of the bundles due to their poorer mechanical properties.
6) The fiber cables might be subject to mechanical stress and fatigue, which leads to failure. The share of *Control and Protection* systems, including *Control and Protection Telecommunications* subsystem, in the Forced Energy Unavailability hours of the HVdc systems worldwide, is 7.8 % between the years 1983–2016 and 7.1 % between 2017–2018 [11]. The two other subsystems included in the figure are *Local Control and Protection* and *Master Control and Protection*.

Wireless control of MMC submodules is proposed in [12], implemented and verified in [13] to solve the issues above. The control method is advanced in [14] so that the submodules experiencing communication errors that last up to hundreds of wireless transmission cycles (tens of milliseconds) can continue their operation as if no error occurred. The method is advanced further in [15] against longer-lasting communication errors (hundreds of milliseconds and more) so that overvoltages, overcurrents, or component failures in the MMC are avoided. The verification of the proposal and advancements in [13]–[15] are all based on a laboratory-scale single-phase MMC with three half-bridge submodules per arm. The experimental setup does not represent a full-scale MMC and its valve hall in terms of the dimensions, the number of communication nodes, and electrical characteristics. Thus, it is unclear how to implement a wireless communication network in a full-scale MMC valve hall. Moreover, if the radiated electromagnetic interference (EMI) from the MMC components coincides with the wireless transmission frequency, higher transmission errors can be expected, which can complicate the wireless control of the submodules. High-power transients resulting from, e.g., electrical arcs and circuit breaker operations, can also interfere with wireless communication [16], [17].

The steady-state operation of full-scale MMCs, which mainly represents the switching of the semiconductors in the submodules, is observed to generate interference up to 1.4 GHz but has significant effects up to 400 MHz in and out of the MMC hall [18], [19]. In another study, the interference in the MMC hall is measured up to 600 MHz [20].

The contributions of this article are twofold. First, a wireless network design is provided for a full-scale MMC based on the wireless control method given in [13]. A theoretical case study is carried out on an example MMC used in HVdc transmission. 5G New Radio (NR) is investigated as the wireless communication solution in the MMC valve hall. Also, antenna placement options in the hall and the related communication link budget and reliability are discussed. Wireless control of the submodules can be enlarged to full-scale MMCs using the proposed wireless network. As the second contribution, the article presents a more realistic radiated EMI environment of a full-scale MMC compared to that in [13] and observes its effects on wireless communication. To this end, firstly, the voltage and current rise rates of the state-of-the-art high-power semiconductors are determined. Then, the radiated EMI (henceforth called just EMI) of two different laboratory-scale submodules are measured while having voltage rise rates similar to that of high-power semiconductors. Also, the EMI of two different dc circuit breakers (DCCBs) are measured with 1 kA peak interrupted current. Lastly, wireless communication packet loss characteristics are measured in the close vicinity of a submodule to observe whether the EMI from the submodule affects the communication. The measurements show that the EMI from the components are confined below 500 MHz (parallel to the results in [18]–[20]) and, thus, a wireless transmission in the multi-GHz range is not affected by the EMI.

The structure of the article is as follows. In Section II, a wireless network is designed for an example full-scale MMC valve hall. In Section III, the EMI spectrum of MMC components is analyzed in a laboratory environment. Section IV contains wireless communication packet loss characteristics when an MMC submodule operates nearby and not. Conclusions are given in Section V.

II. WIRELESS NETWORK DESIGN CASE STUDY IN AN MMC VALVE HALL

In this section, the wireless control method for MMC submodules implemented in [13] and [14] is taken as the basis, and a wireless network is designed for an example full-scale MMC. In the mentioned implementations, the central controller periodically broadcasts the real-time control data to all the submodules in a single data package in the

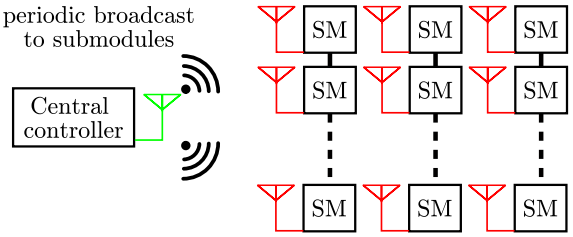

FIGURE 1. The conceptual wireless communication in the MMC valve hall. The connection between the submodules is only electrical.

TABLE 1. Plant parameters to implement wireless communication.

Parameter	Value
Valve hall dimensions (approximately)	114 m × 33 m × 16 m [21]
Number of valve towers in the hall	42 [4]
Total number of submodules	2592 [3]

TABLE 2. Application requirements with wireless control.

Parameter	Value
Transmission cycle (broadcast, unidirect.)	100 µs [13]
Payload (in the DL, excluding any header)	32 B [13]
Packet error rate at the application layer	10^{-2} to 10^{-3} [14]

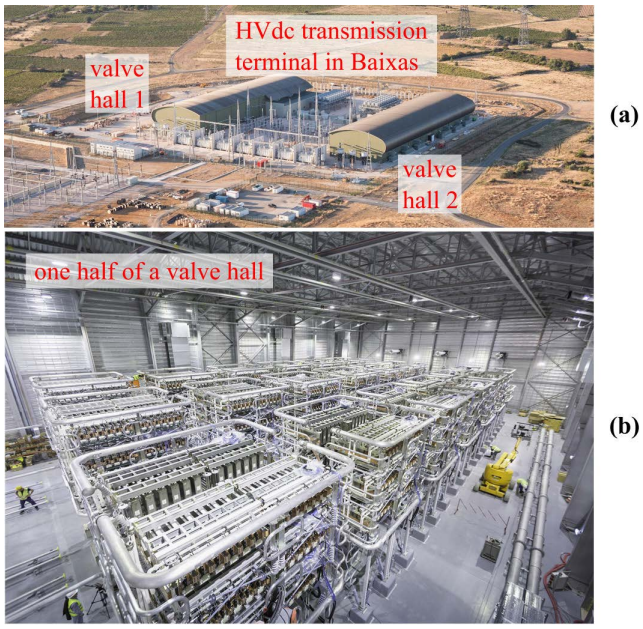

FIGURE 2. MMC valve halls in Baixas, France[2](a) outside (b) inside.

downlink (DL). The communication from the submodules to the central controller, i.e., uplink (UL), is not included in the discussions below as communication in UL is not required to be real-time with the proposed control method in [13]. The conceptual wireless communication network is illustrated in Fig. 1.

The MMC stations used in the HVdc electrical interconnection project between Baixas, France and Santa Llogaia, Spain are chosen as the example application to design the wireless network [4]. The outside and inside views of the MMC station valve hall in Baixas are shown in Fig. 2. Considering other photos of the halls, the hall building looks like a big Faraday cage that attenuates the electromagnetic interference from outside to the valve hall and vice versa. The plant parameters to implement the wireless network are shown in Table 1 and the application requirements are shown in Table 2. Parameters in Table 2 are taken from the laboratory-scale wireless control implementations in [13] and [14], except that 48 % of the payload in Table 2 is spare compared to the mentioned implementations. The transmission cycle, which is set by the cycle time of the central controller algorithms, and the wireless payload in Table 2 result in a 2.56 Mbit s^{-1} raw data rate in the DL.

A. WIRELESS NETWORK IN THE VALVE HALL

MMC submodules control is a time-critical process. It requires low end-to-end latency and high reliability in the control system. The typical sampling period in the control system of the MMCs (and similar power electronics applications) is in the range of 100 µs [13]. The packet error rate (PER) requirement in the application layer for power electronics applications is in the 10^{-8} to 10^{-9} range in [22], which is not reachable with the mentioned sampling (cycle) periods using the current or upcoming wireless communication technology. In order to realize the wireless control of submodules, it is essential to adjust the submodules control such that it can tolerate higher PER values. Using the control method in [14], increasing the suitable PER value at least up to 10^{-2} range is possible, which can be reached by the contemporary low-latency, high-reliability wireless communication solutions without compromising the performance of the MMC. In this sense, 5G NR, which is standardized with 5G release 15, is a promising ultra-reliable low-latency communication (URLLC) solution [23], [24]. The latency bound, packet size, and reliability requirements in a 5G system are set as 1 ms, 32 B, and 99.999 %, respectively, by ITU-R in the IMT-2020 specifications [25]. The packet size and reliability requirements are compatible with the application requirements given in Table 2; however, the latency performance of 5G NR should be investigated further to check whether it can be lowered to the sub-millisecond range.

5G NR operates in frequency bands in two frequency ranges: Frequency Range 1 (FR1) for bands within 410 MHz to 7125 MHz, and Frequency Range 2 (FR2) for bands within 24 250 MHz to 52 600 MHz [26]. 5G has a 10 ms long frame structure in the physical layer. Each frame comprises ten sub-frames with a 1 ms length, and each sub-frame is made up of scalable transmission time intervals (TTIs). One or more consecutive slots allocated to either DL or UL make up a TTI.

[2]https://www.windpowermonthly.com/article/1343089/gallery-france-spain-2gw-hvdc-link
https://www.ree.es/sites/all/inelfe/webscroll.html

Each slot contains 14 orthogonal frequency-division multiplexing (OFDM) symbols, and the length of each slot can be in the range of 125 µs to 1 ms. The length of each OFDM symbol and thus the slot depends on the employed sub-carrier spacing (SCS) frequency, which is 15 kHz (corresponding to 1 ms slot length), 30 kHz, or 60 kHz for operation in FR1, and 60 kHz or 120 kHz (corresponding to 125 µs slot length) for operation in FR2. Hence, the shortest achievable slot duration, T_{slot}, for data transmission with the full 14 OFDM symbols is 250 µs for the operation in FR1 and 125 µs for the operation in FR2. Consequently, 5G NR with a full slot structure cannot respond to the cycle time given in Table 2. On the other hand, 5G NR introduces mini-slot transmissions with 2, 4, or 7 OFDM symbols in the DL. Considering that a single OFDM symbol duration is 17.84 µs and 8.92 µs with SCS equal to 60 kHz and 120 kHz, using mini-slots consisting of 2 OFDM symbols, the shortest achievable T_{slot} can be lowered to 36 µs and 18 µs in the DL with the operation in FR1 and FR2, respectively.

The total physical layer latency, T_L, includes the data processing time intervals in the transmitter (central controller), T_{ptx}, and receivers (submodule controllers), T_{prx}, on top of T_{slot} as [27]

$$T_L = T_{\text{slot}} + T_{\text{ptx}} + T_{\text{prx}}, \tag{1}$$

with no re-transmission or acknowledgment. The processing time depends on several scheduling factors, which are out of the scope of this article, and the processing capabilities of the transceivers. In [28], as a worst-case scenario, T_{ptx} is assumed equal to five times T_{slot} for SCS equal to 60 kHz or 120 kHz for mini-slots with 2 OFDM symbols. Similarly, T_{prx} is assumed equal to five and ten times T_{slot} for SCS equal to 60 kHz and 120 kHz, respectively. The mentioned T_{ptx} and T_{prx} values with the aforementioned T_{slot} end up T_L being equal to roughly 400 µs and 300 µs for the operation in FR1 and FR2, respectively, using frequency division duplex (FDD) mode. (The FDD mode promises shorter processing delay than time division duplex mode as it has shorter alignment delay, i.e., the time from when data becomes available until the next transmission slot starts.) The mentioned T_{ptx} value includes some UL related factors, which are not needed in our scenario. Also, the T_{prx} assumption for 120 kHz SCS is for receiver hardware with basic processing speed. Thus, lower T_{ptx} and T_{prx} values can be obtained. In [29], for example, T_{ptx} and T_{prx} are assumed equal to T_{slot}, which makes T_L equal to 108 µs and 54 µs for SCS equal to 60 kHz and 120 kHz, respectively. Hence, the exact T_L depends on the specific application. Although it does not seem like a straightforward target, the authors do not rule out the possibility of reaching 100 µs transmission cycle with 5G NR, especially with the operation in FR2 with SCS equal to 120 kHz. The key to reaching the target is to reduce T_{ptx} and T_{rtx} to the same range of T_{slot}, which may require advanced transceivers. In case 100 µs transmission cycle is not feasible (e.g., the required hardware costs too much), a workaround would be increasing the cycle time of the central controller algorithms and consequently the transmission cycle, e.g., to 200 µs.

B. ANTENNA PLACEMENT IN THE VALVE HALL AND COMMUNICATION LINK BUDGET

The wireless communication eliminates the workload and costs related to laying out, terminating, and testing the optical-fiber cables between the submodules and the central controller. On the other hand, the placement of the antennas for the central controller and the submodules is introduced as a new task. The reliability of wireless communication depends on the signal-to-interference-plus-noise ratio (SINR) at the receivers, which is dependent on the placement of the transmitter and receiver antennas. Positioning the antennas, the type of antenna to use, and connections between the antenna and the transceiver circuitry require a comprehensive engineering study to minimize the PER and not to present any threat to electrical safety. The critical points for the antenna placement are listed below:

1) The antenna placement should maximize the received radio power considering the other constraints. A line-of-sight (LOS) is desirable.
2) The propagation environment, i.e., MMC valve hall, is complex to model with various conductive elements and metal bars. The assessment of the antenna placement would require detailed design, simulations, and several tests in the valve hall considering the PER.
3) The antennas should not present an electrical safety risk in the high-voltage environment. Hence rod-like and pointy antennas should be avoided. The antennas cannot protrude outside the valve assembly envelope. The electric field redistribution in the hall should be taken into account.

The control room of the MMC in Fig. 2 is placed towards the corner of the rectangular valve hall. The central controller is proposed to have multiple antennas in the hall placed on the ceiling and, if required depending on the antenna placement options below, on the sidewalls of the hall building. The antennas should be placed such that preferably all the submodule antennas have a LOS to a central controller antenna.

An enclosure around the submodule control units is common to provide electromagnetic immunity from nearby interference sources. If the submodule antennas are placed inside the enclosure, the received radio power will be attenuated by the enclosure depending on its material and thickness. We propose placing the antennas outside the enclosures to avoid attenuation.

Three antenna placements options for the submodules and the central controller are considered in this article, where the central controller and submodule antennas are referred to as the transmitter and receiver antennas, respectively:

1) One (set of) antenna per submodule within the submodule structure; one (set of) transmitter antenna on the building ceiling for submodules that are placed face-to-face in two adjoining valve towers and one (set of)

transmitter antenna on the building sidewalls for the submodules of a valve tower that are facing towards the walls;

2) One (set of) antenna per submodule on the valve tower ceiling, the antenna (set) is connected to its submodule over a cable; one (set of) transmitter antenna per tower on the building ceiling;
3) One (set of) antenna per valve tower on the tower ceiling connected to all the submodules in the tower over cables; one (set of) transmitter antenna per tower on the building ceiling.

The options are illustrated in Fig. 3 and compared from different perspectives in Table 3. It is considered that option 3 should be avoided as it presents a single point of communication failure in the valve tower. Option 2 (similar to option 3) has a LOS with a short distance between the transmitter and receiver antennas. However, the electric field in the valve tower might induce high potential difference and harmful currents between the submodule controller and its antenna on the ceiling of the valve tower over the cable connecting them. In order to avoid these, the submodule controller and the antenna need to be galvanically isolated by, e.g., electrical to optical conversion on both ends of the cable, which adds extra latency in the control system. For option 1, submodules facing the building walls can have a LOS to transmitter antennas placed on the walls. Also, for submodules placed face-to-face in two adjoining valve towers, LOS to a transmitter antenna placed diagonally on the ceiling seems possible. However, a detailed investigation is required to ensure LOS for all the submodules in the valve tower. Considering Fig. 2 and the dimensions of the valve hall in Table 1, the distances between the transmitter and receiver antennas are estimated at around 5 m in options 2 and 3. The maximum distance is estimated at around 10 m for option 1.

5G NR operates in frequency bands in two frequency ranges, FR1 and FR2, as expressed in the previous subsection. A great majority of the specified bands are reserved for 5G NR operation. Thus, interference from the ISM bands, which are reserved internationally for industrial, scientific, and medical (ISM) purposes and usually unlicensed, is highly unlikely for 5G NR unless it operates in one of the few frequency bands that coincide with the ISM bands, e.g., *n53*.

The 5G NR link budget for the antenna placement option 1 is calculated in an online tool [30]. (Options 2 and 3 have a shorter distance between the transmitter and receiver antennas.) The parameters for the calculations are given in Table 4. Additionally, *Indoor Hotspot 3D-InH LOS + NLOS* propagation model is chosen. For FR1 operation, the 5G frequency band with FDD mode and the highest transmission center frequency -*n7*- is selected. The resulting SINRs are 50 dB and 30 dB for transmission in FR1 and FR2. The SINR values are so high that the resulting PER is low enough to satisfy the 10^{-2} to 10^{-3} requirement in Table 2 for almost any modulation and coding scheme [28], [31]. As a result, option 1 seems like a better alternative considering all the factors mentioned above and given in Table 3. The definite choice would require

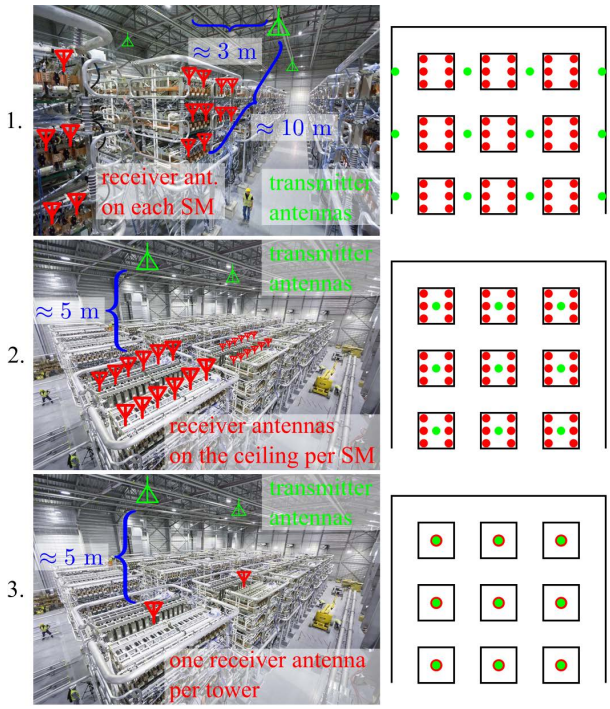

FIGURE 3. Three antenna placement options in the valve hall (left), illustration of the placements looking towards the valve towers from the ceiling (right). In the illustrations, the black squares represent the valve towers, green and red dots represent the transmitter and receiver antennas, respectively.

detailed analyses and tests to verify the SINR calculations, PER, and whether the errors can be compensated by other measures like the autonomous submodule controllers [14].

III. EMI SPECTRUM ANALYSES OF MMC COMPONENTS

In the previous section, a 5G NR communication system operating in the multi-GHz range is evaluated for wireless communication in the MMC valve hall. This section analyzes the EMI of two different submodules and two different DCCBs to identify whether they coincide with the 5G NR transmission frequency bands. For this purpose, measurements are performed in a laboratory environment. In all the measurements, the following infrastructure is shared. The electromagnetic (EM) spectrum is analyzed with a Rohde&Schwarz FSH8 spectrum analyzer. A BicoLOG 5070 X biconical antenna and an MVG QH800 open boundary quad-ridge horn antenna are used to measure EMI in 50 MHz to 700 MHz and 0.8 GHz to 6 GHz frequency ranges, respectively. The spectrum analyzer is set to record the maximum measured signal during the measurements, and the measurements remained for 10 minutes for the submodules.

EMI from power electronics applications is dependent on the power semiconductor switching characteristics. Table 5 shows the dynamic performance test ratings and rise rates of the voltage and current (dv/dt and di/dt) for the state-of-the-art insulated-gate bipolar transistors (IGBTs) used in high-power applications. The current and voltage rise rates

TABLE 3. Evaluation of antenna placement options in the valve hall.

	Option 1	Option 2	Option 3
Radio signal reception	The location of the receiver antenna has limited flexibility in terms of good signal reception. The receiver and transmitter antennas might have a LOS or not.	The receiver antennas are placed on the tower ceiling to obtain a LOS with the transmitter antenna. Some limitations on the placement might occur due to the footprint of many antennas.	The receiver antenna is placed on the tower ceiling to obtain the best signal reception and a LOS with a transmitter antenna.
Electrical isolation and latency	The submodule controllers are electrically isolated from each other.	The receiver antenna outputs need to be converted from electrical to, e.g., optical to provide galvanic isolation between the antenna and the submodule controller and back to electrical in the submodule controller, adding extra latency in the control system.	The single receiver antenna output needs to be converted from electrical to, e.g., optical to provide galvanic isolation between the antenna and the submodule controllers and back to electrical in the submodule controllers, adding extra latency in the control system.
Submodule assembly	The entire assembly and test of the submodule can be completed in the factory with all the communication system components installed.	The antenna connections should be done on-site and need cable layout within the tower. The submodules need to be tested after the antenna connections are made.	The antenna connection should be done on-site and needs a cable layout within the tower. The submodules need to be tested after the antenna connections are made.
Wireless data characteristics	Independent wireless packet losses and delay in each submodule with some correlation depending on the antenna placements.	Independent wireless packet losses and delay in each submodule with some correlation depending on the antenna placements.	The same wireless packet losses and delay in each submodule of a tower assuming the same attenuation after the reception of the signal until each submodule controller.
Maintenance of the submodule	Shorter time for submodule replacement as the receiver antenna is a part of the submodule structure.	Longer time for submodule replacement due to the receiver antenna connection.	Longer time for submodule replacement due to the receiver antenna connection.
Cost	One (set of) antenna cost per submodule (receiver), four (set of) antenna cost per three adjoining towers (transmitter).	One (set of) antenna cost per submodule (receiver) and one (set of) antenna cost per tower (transmitter), electrical to optical converters, cabling between the antenna and the submodule, and commissioning after the connection.	Two (set of) antenna cost per tower (transmitter and receiver), electrical to optical converters, splitters, amplifiers, cabling between the antenna to each submodule, and commissioning after the connection.

TABLE 4. 5G NR link budget calculation parameters.

Parameter	FR1	FR2
SCS frequency (kHz)	60	120
Transmission center frequency (MHz)	2600	26000
Number of resource blocks	65	32
Full path loss (dB)	77	97
Transmission power (dBm)	30	
Noise (dB)	20	
Cell radius (m)	3	
Transmitter antenna height (m)	15	
Receiver antenna height (m)	5	

TABLE 5. High-power IGBTs voltage and current rise rates.

Device	V_{CES} (V)	V_{CC} (V)	dv/dt (V/ns)	I_C (A)	di/dt (A/ns)
5SNA 2000K451300[a]	4500	2800	3.94	2000	3.02
CM1500HC-66R[b]	3300	1800	6.00	1500	4.00
FZ1500R33HE3[c]	3300	1800	5.14	1500	3.43

a: ABB, b: Mitsubishi Electric, c: Infineon.

are calculated using the rise and fall times of the current, respectively, stated in the datasheets of the IGBTs with the given test conditions [32]. It is considered that the table gives the correct order of magnitude for the rates, even if not the correct values, for the submodules in full-scale MMCs.

A. FULL-BRIDGE SUBMODULE WITH SI MOSFETs

The experimental setup is shown in Fig. 4. The full-bridge submodule comprises IRFP4768PbF silicon MOSFETs (the same MOSFETs used in the experimental study in [13]) and two parallel-connected 30 µF film capacitors on the dc-side. The submodule electrical circuit and the controller are assembled on a single printed circuit board. The controller is based on the Xilinx Zynq-7000 system-on-chip. The submodule is connected to a voltage source on the dc-side by a twisted pair of cables. The ac-side is connected to variable resistors by a twisted pair of cables. Measurements are taken when the submodule is enclosed in an aluminum 19-inch rack and not enclosed. When the submodule is enclosed, the dc- and ac-side cable pairs are shielded, and the shields are earthed on both ends. Otherwise, no shield is used. When used, the aluminum rack is earthed via the cabinet. The experiments are performed with 100 kHz switching frequency and unipolar pulse-width modulation with 0.95 amplitude modulation index. The voltage measurements are taken directly from the MOSFET terminals. During the experiments, no other high-power equipment is operated nearby.

1) RESULTS

Combinations of two dc-side voltages, 100 V and 150 V, and four ac-side peak currents, 0 A, 10 A, 20 A, and 30 A, are experimented. The results are tagged in the figures as

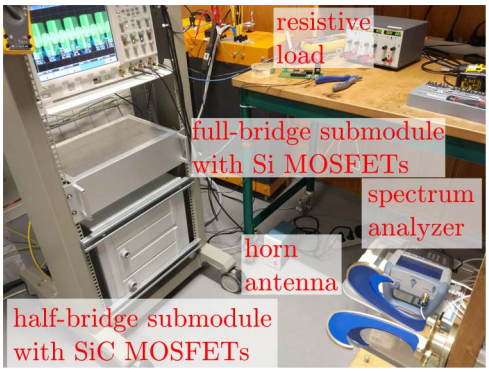

FIGURE 4. Experimental setup of the submodules: full-bridge submodule with Si MOSFETs enclosed in an aluminum 19-inch rack, half-bridge submodule with SiC MOSFETs enclosed in an aluminum enclosure.

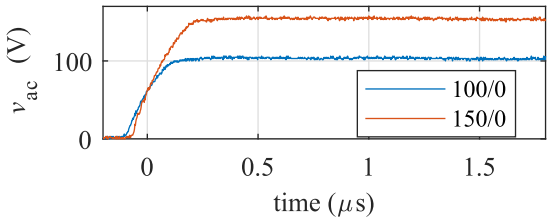

FIGURE 5. Ac-side voltage waveforms of active cases 100/0 and 150/0 right after the turn-on of the MOSFETs that result in positive ac-side voltage.

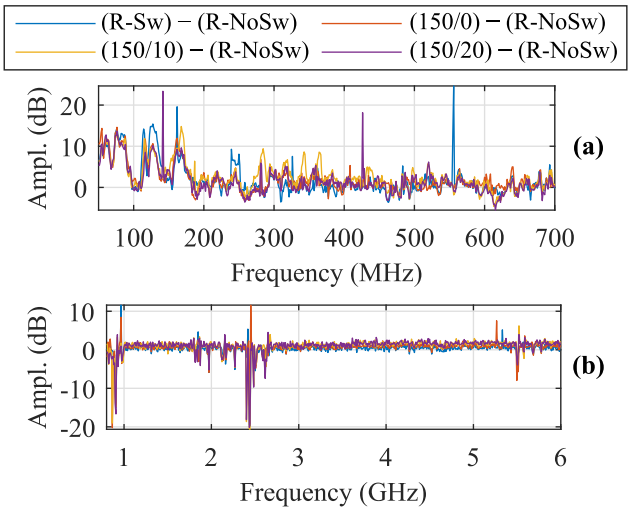

FIGURE 6. EMI differences from *R-NoSw* in 50 MHz to 700 MHz (a) and 0.8 GHz to 6 GHz (b) ranges for 150 V dc-side voltage active cases, with aluminum enclosure.

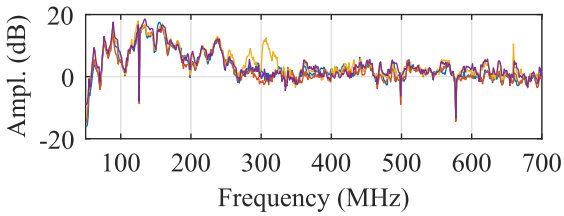

FIGURE 7. EMI differences from *R-NoSw* in 50 MHz to 700 MHz range for 150 V dc-side voltage active cases, no aluminum enclosure. The high-frequency spectrum is similar to Fig. 6.(b). The legend of the figure is the same as in Fig. 6.

volts/amperes according to the voltage and peak current level used in the experiment. For instance, 100/10 stands for the experiment run with 100 V dc-side voltage and 10 A peak ac-side current. *R-NoSw* is for the reference experiment in which the converter and the controller are not energized. *R-Sw* is for the reference experiment in which the controller is energized, and the MOSFETs are switching, but the converter has 0 V dc-side voltage. The experiments with nonzero dc-side voltage are referred to as *active cases* hereafter. Fig. 5 shows the submodule ac-side voltage v_{ac} of the active cases 100/0 and 150/0 right after the turn-on of the respective MOSFETs that result in positive ac-side voltage. 100/0 and 150/0 have smooth waveforms with $\approx 0.5\,\mathrm{V/ns}$ and $\approx 0.6\,\mathrm{V/ns}$ voltage rise rates, respectively. No snubber is used for the MOSFETs.

To distinguish the EMI of different test cases, the differences in the EMI of the active cases from the reference *R-NoSw* are shown in Figs. 6 and 7 for the 150 V dc-side voltage active cases with and without the aluminum rack, respectively. The figures reveal that as soon as the switching starts in the submodule, even with zero dc-side voltage, EMI in the low-frequency range from 50 MHz to 300 MHz is 10 dB to 20 dB higher than *R-NoSw*. Having a nonzero dc-side voltage or higher ac-side current does not affect the EMI particularly. Compared to the *R-NoSw* reference, the higher EMI is mainly related to the switchings and the driver circuit. Comparing Figs. 6.(a) and 7, the aluminum rack decreases the interference from 100 MHz to 300 MHz up to 10 dB. In the high-frequency range, there are some outliers from 800 MHz to 900 MHz, 2.4 GHz to 2.7 GHz, and 5.2 GHz to 5.6 GHz; however, no continuous frequency range has higher interference than the reference. The outliers in the 800 MHz to 900 MHz range are considered sourced from GSM, 3G, and 4G networks, and those in 2.5 GHz to 2.7 GHz are from 4G networks in Sweden [33]. The outliers in the 2.4 GHz to 2.5 GHz and 5.2 GHz to 5.6 GHz ranges are considered sourced from the nearby WLAN networks. Consequently, the experimented full-bridge submodule does not affect the EM spectrum above 300 MHz. It should be noted that the voltage rise rates in the experiments are an order of magnitude smaller than those in Table 5.

B. HALF-BRIDGE SUBMODULE WITH SiC MOSFETs

The experimental setup is shown in Fig. 4. The half-bridge submodule comprises a CAS300M12BM2 half-bridge silicon-carbide MOSFET module and two parallel-connected 680 µF film capacitors. The submodule is enclosed in an aluminum enclosure. The half-bridge driver is placed in the enclosure, and it has optical fiber switching pulse inputs from the submodule controller, which is placed out of the enclosure. The controller is based on the Xilinx Zynq-7000 system-on-chip. The submodule and the controller are galvanically isolated. The submodule is connected to a voltage source on

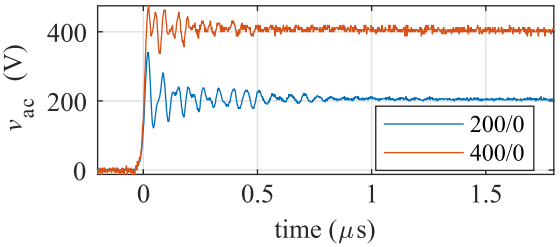

FIGURE 8. Ac-side voltage waveforms of active cases 200/0 and 400/0 right after the turn-off of the low-side MOSFET.

the dc-side by an unshielded twisted pair of cables. The ac-side is connected to variable resistors with a shielded pair of cables. The cable shield is earthed on both ends. The sub-module enclosure is earthed via the cabinet. The experiments are performed using sinusoidal pulse-width modulation with 833 Hz switching frequency and 0.95 amplitude modulation index.

1) RESULTS

Combinations of two dc-side voltages, 200 V and 400 V, and four ac-side peak current levels, 0 A, 10 A, 20 A, and 30 A, are experimented. The results are tagged in the figures as explained in the previous subsection. Test case *R* stands for the reference case in which the converter has 0 V dc-side voltage, but all the control circuits and auxiliary setup are up and running. In Fig. 8, the ac-side voltage enlarged waveform of 200/0 and 400/0 measurements right after the low-side MOSFET turn-off are compared. The active cases with 200 V and 400 V dc-side voltages have $\approx$ 14 V/ns and $\approx$ 19 V/ns voltage rise rates, respectively. The values are higher than those in Table 5. Oscillations in the waveforms are observed with peak-to-peak voltages of 220 V and 125 V for 200/0 and 400/0 active cases, respectively. The oscillations are fundamentally due to the resonant behavior of the parasitic inductance on the current path of the MOSFETs and the parasitic capacitance of the MOSFETs. The current rise rates of 200/30 and 400/30 active cases are 0.37 A/µs and 0.52 A/µs, respectively. They are much smaller than those in Table 5. The current rise rates refer that the experimental setup has a parasitic inductance in the hundreds of µH range.

The differences in the EMI of the active cases from the reference case *R* are shown in Figs. 9 and 10 for the 200 V and 400 V dc-side voltages, respectively. The low-frequency spectra from 50 MHz to 700 MHz present more diversity than the high-frequency spectra from 0.8 GHz to 6 GHz in both figures. A detailed investigation reveals that the differences are mostly individual low-bandwidth outliers in a single active case. The number and amplitudes of outliers in the 200 V cases are more than in the 400 V cases. This difference can be verified by comparing the variances of the active cases shown at the top of the figures. The higher peak-to-peak amplitude of the switching oscillations in 200 V active cases is considered to cause more and higher amplitude EMI outliers. There are a few noticeable frequencies around

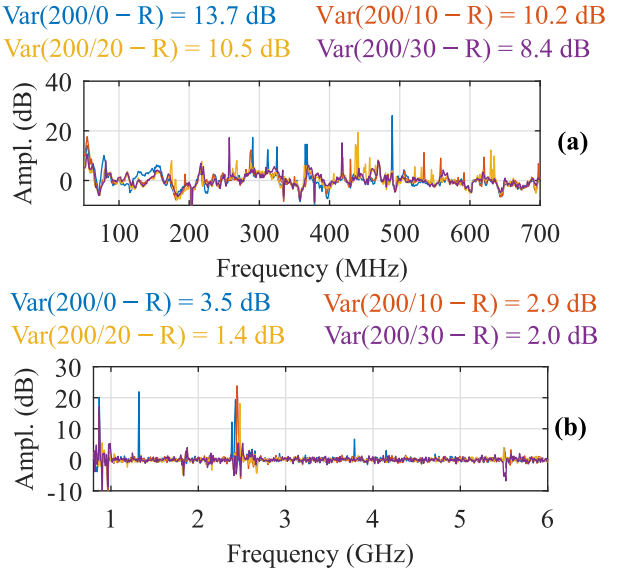

FIGURE 9. EMI differences from *R* in 50 MHz to 700 MHz (a) and 0.8 GHz to 6 GHz (b) ranges for 200 V dc-side voltage active cases.

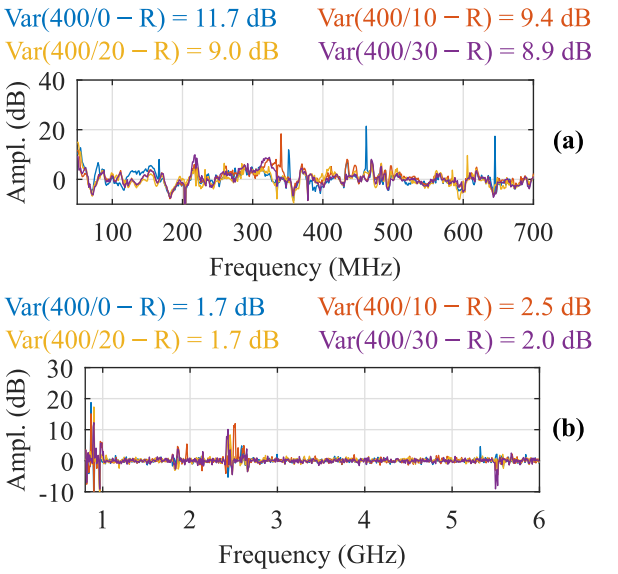

FIGURE 10. EMI differences from *R* in 50 MHz to 700 MHz (a) and 0.8 GHz to 6 GHz (b) ranges for 400 V dc-side voltage active cases.

which both the 200 V and 400 V cases have increased interference levels altogether by more than 5 dB. This behavior can be seen around 50 MHz and 470 MHz, but there is no relation between the increased ac-side current amplitude and the interference level. It is important to note that the LTE450 network is present at around 470 MHz [33]. In the high-frequency spectra, there are several outliers in the 800 MHz to 900 MHz and 2.4 GHz to 2.7 GHz ranges and around 5.5 GHz, which are considered originating from the GSM, 3G, 4G, and WLAN networks as detailed previously.

The measurements are repeated with an unmounted enclosure lid. The differences in the EMI of the active cases from

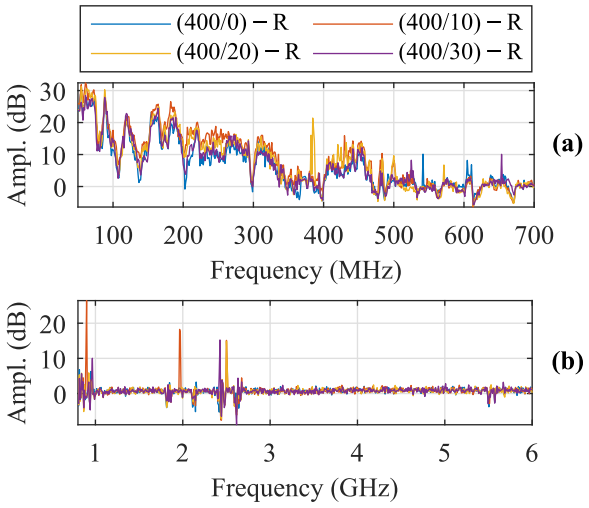

FIGURE 11. EMI differences from *R* in 50 MHz to 700 MHz (a) and 0.8 GHz to 6 GHz (b) ranges for 400 V dc-side voltage active cases with demounted enclosure cover.

the reference case are shown in Fig. 11 for 400 V dc-side voltage. All the active cases have up to 20 dB higher interference than the reference in 50 MHz to 350 MHz and 400 MHz to 500 MHz ranges. The interference amplitude decreases with the frequency. When Figs. 10 and 11 are compared, the interference from the submodule is confined mostly below 500 MHz. In the high-frequency range, individual outliers are seen in the active cases in 0.8 GHz to 1 GHz, 1.8 GHz to 2.2 GHz, 2.4 GHz to 2.7 GHz ranges, and around 5.5 GHz. Interference in the 1.8 GHz to 2.2 GHz range is considered to be originating from GSM, 3G, and 4G networks [33]. The other frequency ranges were explained previously. These results are promising indications that the wireless communication in the multi-GHz frequency band would function properly with no harmful interference from the submodule switchings even without proper EM shielding.

C. DC CIRCUIT BREAKERS

MMCs can be used to form HVdc grids. The reliable operation of HVdc grids requires protection against dc-side faults. MMC-HVdc terminals constructed with half-bridge submodules cannot control and limit the dc fault current and requires DCCBs for the protection [34]. AC circuit breakers rely on the current zero-crossing of the ac fault current to interrupt. However, dc fault currents do not have a natural current zero-crossing, and specialized DCCBs are needed to protect dc systems. A solution is the general DCCB structure depicted in Fig. 12. As shown in [35], the implementation of the general DCCB structure only affects the internal commutation processes between the parallel paths for the current, as in Fig. 12. Still, the internal commutation processes can cause different EMI throughout the operation of the DCCB because of the underlying physical phenomena and the switching transients during the commutations. Although it is unlikely that the DCCBs are placed directly in MMC valve halls and affect the

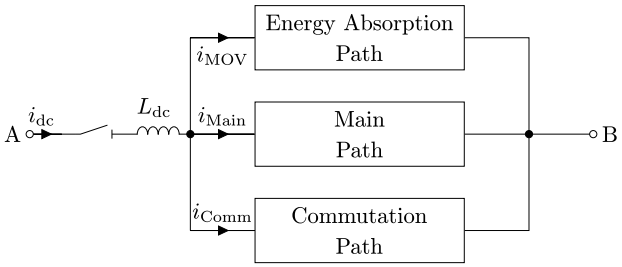

FIGURE 12. General dc circuit breaker structure.

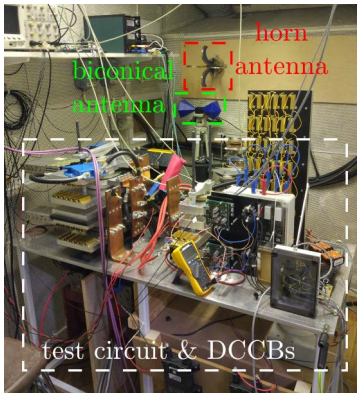

FIGURE 13. Experimental setup of the solid-state and EAR DCCBs.

EM spectrum in the halls significantly, the EMI of DCCBs are still considered of interest as they would be placed in the same switchyard of the MMC station [36].

Two DCCBs, which operate similarly to the two major types of DCCBs, are used in dc interruption tests: a solid-state DCCB based on an integrated gate-commutated thyristor without snubber and an enhanced active resonant (EAR) DCCB based on a triggered vacuum gap as described in [37]. As in ac circuit breakers, the core component of EAR DCCBs, the triggered vacuum gap, operates with an electric arc discharge enclosed by the device. The experimental setup is shown in Fig. 13. The current i_{dc} and voltage v_{dc} as seen by the dc system at the terminals of the DCCB measured in experiments at 1 kA are given in Fig. 14. The switching transient of v_{dc} indicates that injection-type DCCBs like the EAR DCCB commutate slower than semiconductor-based DCCBs. The maximum di/dt and dv/dt observed, considering the internal currents measured, are 61.0 A/µs and 14.3 V/µs and 80.7 A/µs and 137.8 V/µs for the EAR and solid-state DCCB, respectively. The EMI differences after the operation of DCCBs than before the operation of DCCBs are shown in Fig. 15. In both cases, the interference generated by the operation of the DCCBs is marginal, and it is observed that the primary source of EMI is the auxiliary circuits such as switching dc power supplies.

D. DISCUSSION

The EMI measurements of MMC submodules with voltage rise rates up to 19 V/ns and current rise rates up to 0.52 A/µs

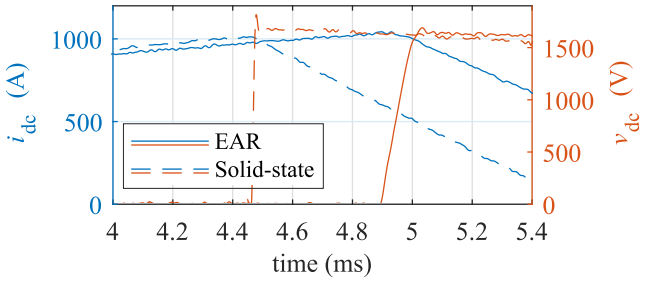

FIGURE 14. The internal currents and the voltage of the DCCB measured in dc interruption tests at 1 kA.

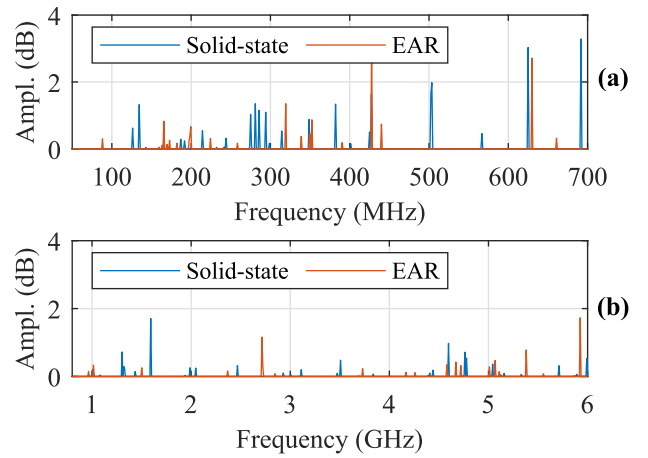

FIGURE 15. The EMI differences before and after the operation of DCCBs operated at 1 kA between 50 MHz to 700 MHz (a) and 0.8 GHz to 6 GHz (b).

resulted in the interference from the submodules being confined below 500 MHz. The measurements with solid-state and EAR DCCBs have a marginal effect in the sub-GHz range and above. It is hypothesized that a wireless communication link with a transmission center frequency in the multi-GHz range, as proposed in Section II-A and as in [13], would not suffer from the EMI generated by the MMC submodules and DCCBs operating with similar parameters to those experimented in the previous subsections. The hypothesis will be experimented with in the next section.

IV. WIRELESS COMMUNICATION PACKET LOSS CHARACTERISTICS

In order to verify the hypothesis raised in Section III-D, packet losses of a wireless communication link are measured in the presence of the EMI generated by the specified half-bridge submodule in Section III-B, and the results are compared to a reference measurement. The measurement setup and the surrounding environment are sketched in Fig. 16. The submodule and the receiver are fixed, whereas the transmitter is placed 2, 4, 8, and 16 m apart from the submodule in different measurement campaigns. The transceivers are in LOS. Several electrical motors, metal structures, frames, bench legs, and fences are in the surrounding environment. Computers and bench-top equipment are placed on the benches and attached frames. Metal pipes are along with

TABLE 6. Wireless communication parameters.

Protocol	IEEE 802.11a	Transmiss. period	100 µs
Data rate	18 Mbit/s	Transmiss. power	10 dBm
Modulation	QPSK	Transmiss. center freq.	5825 MHz
Payload	32 B	Transmiss. bandwidth	20 MHz

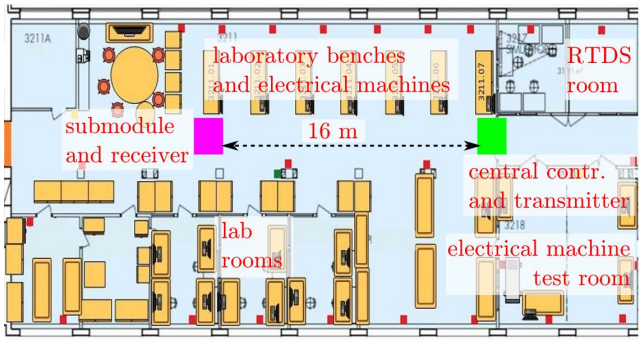

FIGURE 16. The sketching of the experimental setup for wireless communication packet loss measurements and the surrounding environment.

the ceiling, and the floor material is semiconducting. Power panels with metal covers are placed on the sidewalls. All the surroundings present a unique EM wave propagation environment, which probably does not match a full-scale MMC hall. However, some resemblance can be argued with the metal frames, pipes, and power panels on the walls. It is considered that in an MMC hall, antenna placements with LOS and five to ten meters of distance might be realistic, as proposed in Section II-B. From the electrical rating point-of-view, the voltage rise rate of the employed submodule is higher than that of the considered full-scale MMCs, but the current rise rate is much smaller, as expressed in Section III-B1.

The wireless transceivers are based on WARP v3 kits. WARP project offers a reference IEEE 802.11 orthogonal frequency-division multiplexing physical layer (PHY) and a distributed coordination function medium access control (MAC) design [38]. In this study, carrier-sense and random backoff mechanisms of the MAC layer are disabled, and PHY is used for wireless communication. The wireless transmitter is connected to a controller serving as the central controller of an MMC. The wireless receiver is connected to the submodule controller as in Section III-B. The submodule controller is reached remotely during the measurements to observe the number of packet losses. The measurements are conducted in a stationary propagation environment. The employed wireless communication parameters are listed in Table 6. The transmission center frequency is towards the end of the 5 GHz band, and it is the same frequency employed in the previous experiments in [13] and [14]. Nevertheless, a majority of the frequency bands in FR1 are defined below 3 GHz for 5G NR [39].

The submodule is energized and de-energized consecutively for 10-minute periods during the measurements. When energized, the active case 400/10 is implemented.

TABLE 7. Wireless communication packet losses, 8 m distance.

Measurement	Loss length (in consecutive packets)					
	1	2	3	4	5	6
	7	8	9	10	10+	**PER***
400/10 – 1	7079	104	3	0	0	0
	0	0	0	0	0	**1.22**
R – 1	6936	91	3	3	1	0
	0	0	0	0	0	**1.19**
400/10 – 2	12380	276	27	3	0	0
	0	0	0	0	0	**2.17**
R – 2	8515	157	6	0	0	0
	0	0	0	0	0	**1.48**
400/10 – 3	10891	231	19	4	0	0
	0	0	0	0	0	**1.90**
R – 3	9953	197	9	2	0	0
	0	0	0	0	0	**1.73**
400/10 – 4	12848	356	24	3	0	0
	0	0	0	0	0	**2.27**
R – 4	11516	269	16	6	0	0
	0	0	0	0	0	**2.02**
400/10 – 5	12335	303	18	2	1	1
	0	0	0	0	0	**2.17**
R – 5	12962	312	20	3	2	0
	0	0	0	0	0	**2.28**
400/10 – 6	12161	289	16	2	1	0
	0	0	0	0	0	**2.13**
R – 6	11105	252	20	1	0	0
	0	0	0	0	0	**1.95**
Mean 400/10	11282	260	18	2	0	0
	0	0	0	0	0	**1.98**
Mean R	10165	213	12	3	1	0
	0	0	0	0	0	**1.77**
SD† 400/10	2161	86	8	1	1	0
	0	0	0	0	0	0.39
SD† R	2178	81	7	2	1	0
	0	0	0	0	0	0.40

* Packet error rate $\left(\times 10^{-3}\right)$. 6×10^6 packets are transmitted in 10 minutes when T_s is 100 μs.
† Standard deviation.

When de-energized, the reference *R* is repeated with the additional presence and operation of wireless transceivers. Table 7 shows the number of packet losses with specified loss lengths in consecutive packets for each 400/10 and *R* measurement with 8 m distance between the wireless transmitter and receiver. The other tables corresponding to 2, 4, and 16 m distances are not shown for brevity. The number of packet losses for each loss length and the PER are similar for the 400/10 and the *R* measurements in each campaign. The mean and standard deviation of the packet losses are close to each other. The packet losses are dependent on the distance between the transceivers, as expected. However, considering each campaign in itself, there is no indication that the EMI from the submodule causes more packet losses. Thus, the measurement results confirm that the EMI from the submodule does not deteriorate wireless communication held in the multi-GHz range.

V. CONCLUSION

This article first exemplifies a wireless network design on a full-scale MMC used for HVdc transmission. Considering the size of the MMC valve hall, the number of submodules, and MMC control system parameters, the 5G NR solution seems promising to provide the required broadcast cycle. Three options for wireless antenna placements in the MMC hall are envisioned and compared in different aspects. Central controller antennas on the ceiling and sidewalls of the hall building and one (set of) antenna per submodule integrated with the submodule structure might be preferential, but the definite choice requires more detailed analysis and experiments. The second part of the article measures the EMI of two different laboratory-scale MMC submodules and DCCBs. The interference from the submodules in the steady-state operation is confined below 500 MHz. Interference from the experimented solid-state and EAR DCCBs is marginal in the whole frequency spectrum. Later, the wireless communication errors are characterized in the vicinity of the half-bridge submodule that operates with a higher voltage rise rate than a full-scale MMC submodule. The results verified that the generated EMI of the submodule does not interfere with the employed wireless communication with 5825 MHz transmission center frequency. This is a promising result to expect similar behavior from the full-scale MMC submodules. Several other points require further investigation to ensure that the EMI from the MMC components does not deteriorate wireless communication. Some of them are the submodule measurements with higher current and rise rates, the EMI from electrical arcs in open space, and shoot-through faults, i.e., the faults over a low resistance path between the submodule capacitor positive and negative terminals. Also, the placement of components in a full-scale MMC hall presents a unique propagation environment and should be engineered accordingly to provide proper wireless communication.

ACKNOWLEDGMENT

The authors would like to thank Seyed Samie Mostafavi for his contributions in Section II-A and the Division of Electromagnetic Engineering at KTH Royal Institute of Technology for sharing the MVG QH800 antenna.

REFERENCES

[1] S. Debnath, J. Qin, B. Bahrani, M. Saeedifard, and P. Barbosa, "Operation, control, and applications of the modular multilevel converter: A review," *IEEE Trans. Power Electron.*, vol. 30, no. 1, pp. 37–53, Jan. 2015.
[2] H.-J. Knaak, "Modular multilevel converters and HVDC/FACTS: A success story," in *Proc. 14th Eur. Conf. Power Electron. Appl.*, Birmingham, U.K., 2011, pp. 1–6.
[3] S. Dennetiere, S. Nguefeu, H. Saad, and J. Mahseredjian, "Modeling of modular multilevel converters for the France-Spain link," in *Proc. Int. Conf. Power Syst. Transients*, Vancouver, BC, Canada, 2013, pp. 1–3.
[4] Inelfe. *Electrical Interconnection Between Baixas—Santa Llogaia*, Accessed: Nov. 1, 2021. [Online]. Available: https://www.inelfe.eu/en/projects/baixas-santa-llogaia
[5] L. Brand, "Testing and commissioning of VSC HVDC systems," Cigre, Paris, France, Tech. Rep. 697, Aug. 2017.
[6] M. Daby, "Consultancy support for OFGEM's cost assessment of the proposed NSL interconnector," Atkins, Epsom, U.K., Tech. Rep. SN01115634, Apr. 2016. [Online]. Available: https://www.ofgem.gov.uk/sites/default/files/docs/2016/10/nsl_fpa_atkins_report_redacted.pdf
[7] D. Westermann, D. Van Hertem, G. Real, and T. Rauhala, "Voltage source converter (VSC) HVDC for power transmission—Economic aspects and comparison with other AC and DC technologies," Cigre, Paris, France, Tech. Rep. 492, Apr. 2012.

[8] R. Johnson and G. Wolf, "Refurbish rather than replace: Resuscitating aging HVdc and FACTS projects," *IEEE Power Energy Mag.*, vol. 14, no. 2, pp. 22–31, Mar. 2016.
[9] T. J. Stott and P. R. Couch, "Optical communications network for high voltage direct current power transmission," French Patent 2013 178 249 Al, Dec. 5, 2013.
[10] J. Allaire, "Fire aspects of HVDC thyristor valves and valve Halls," Cigre, Paris, France, Tech. Rep. 136, Feb. 1999.
[11] M. Bennett and L. Crowe, "A survey of the reliability of HVDC systems throughout the world during 2017–2018," in *Proc. Cigre E-Session*, Paris, France, 2020, pp. 1–13.
[12] B. Ciftci, J. Gross, S. Norrga, L. Kildehøj, and H.-P. Nee, "A proposal for wireless control of submodules in modular multilevel converters," in *Proc. 20th Eur. Conf. Power Electron. Appl.*, Riga, Latvia, Sep. 2018, pp. 1–10.
[13] B. Ciftci, S. Schiessl, J. Gross, L. Harnefors, S. Norrga, and H.-P. Nee, "Wireless control of modular multilevel converter submodules," *IEEE Trans. Power Electron.*, vol. 36, no. 7, pp. 8439–8453, Jul. 2021.
[14] B. Ciftci, L. Harnefors, X. Wang, J. Gross, S. Norrga, and H.-P. Nee, "Wireless control of modular multilevel converter submodules with communication errors," *IEEE Trans. Ind. Electron.*, early access, Nov. 13, 2021, doi: 10.1109/TIE.2021.3125664.
[15] B. Çiftçi, L. Harnefors, X. Wang, J. Gross, S. Norrga, and H.-P. Nee, "Wireless control of modular multilevel converter autonomous submodules," in *Proc. 23rd Eur. Conf. Power Electron. Appl.*, Ghent, Belgium, Sep. 2021, pp. 1–10.
[16] A. Abdrabou and A. M. Gaouda, "Uninterrupted wireless data transfer for smart grids in the presence of high power transients," *IEEE Syst. J.*, vol. 9, no. 2, pp. 567–577, Jun. 2015.
[17] C. Kländer and J. L. ter Haseborg, "Effects of high-power and transient disturbances on wireless communication systems operating inside the 2.4 GHz ISM band," in *IEEE Int. Symp. Electromagn. Compat.*, Fort Lauderdale, FL, USA, Jul. 2010, pp. 359–363.
[18] J. Zhang, T. Lu, W. Zhang, H. Shen, and Z. Yang, "Frequency-time domain characteristics of radiated electric fields in a multi-terminal MMC-HVDC station," *IEEE Access*, vol. 7, pp. 99937–99944, 2019.
[19] J. Zhang, T. Lu, W. Zhang, J. Xu, and W. Li, "Measurement and analysis of radiated disturbance characteristics of ±320 kV modular multilevel converter system," *IEEE Access*, vol. 7, pp. 10028–10036, 2019.
[20] W. Chen, L. Jia, L. Yu, and M. Li, "Measurement and analysis of electromagnetic disturbances in 500 kV DC converter station," in *Proc. China Int. Conf. Electr. Distribution*, Shanghai, China, Sep. 2012, pp. 1–5.
[21] Google. *Station De Conversion HVDC Baixas*. Accessed: Nov. 1, 2021. [Online]. Available: https://www.google.com/maps/42.7311046,2.8012399,261m/data=!3m1!1e3
[22] M. Luvisotto, Z. Pang, and D. Dzung, "Ultra high performance wireless control for critical applications: Challenges and directions," *IEEE Trans. Ind. Informat.*, vol. 13, no. 3, pp. 1448–1459, Jun. 2017.
[23] *5G for Connected Industries and Automation*, 5G Alliance for Connected Industries and Automation, Frankfurt, Germany, Feb. 2019. [Online]. Available: https://5g-acia.org/wp-content/uploads/5G-ACIA_WP_5G-for-Connected-Industries-and-Automation-Second-Edition_SinglePages.pdf
[24] X. Jiang, M. Luvisotto, Z. Pang, and C. Fischione, "Reliable minimum cycle time of 5G NR based on data-driven channel characterization," *IEEE Trans. Ind. Informat.*, vol. 17, no. 11, pp. 7401–7411, Nov. 2021.
[25] *Guidelines for Evaluation of Radio Interface Technologies for IMT-2020*, document IMT-2020.EVAL, International Telecommunication Union, Jun. 2017.
[26] O. Liberg, M. Sundberg, Y.-P. E. Wang, J. Bergman, J. Sachs, and G. Wikström, "NR URLLC," in *Cellular Internet of Things*, 2nd ed. New York, NY, USA: Academic, 2020, pp. 515–562. [Online]. Available: https://www.sciencedirect.com/science/article/pii/B978008102902200011
[27] H. Ji, S. Park, J. Yeo, Y. Kim, J. Lee, and B. Shim, "Ultra-reliable and low-latency communications in 5G downlink: Physical layer aspects," *IEEE Wireless Commun.*, vol. 25, no. 3, pp. 124–130, Jun. 2018.
[28] O. Liberg, M. Sundberg, Y.-P. E. Wang, J. Bergman, J. Sachs, and G. Wikström, "NR URLLC performance," in *Cellular Internet of Things*, 2nd ed. New York, NY, USA: Academic, 2020, pp. 563–599. [Online]. Available: https://www.sciencedirect.com/science/article/pii/B9780081029022000121
[29] *UP Latency in NR*, document R2-1711550, Generation Partnership Project, Oct. 2017.
[30] 5G Tools for RF Wireless. *5G NR Link Budget Calculator*. Accessed: Dec. 25, 2021. [Online]. Available: https://5g-tools.com/5g-nr-link-budget-calculator/
[31] M. Sybis, K. Wesolowski, K. Jayasinghe, V. Venkatasubramanian, and V. Vukadinovic, "Channel coding for ultra-reliable low-latency communication in 5G systems," in *Proc. IEEE 84th Veh. Technol. Conf. (VTC-Fall)*, Montreal, QC, Canada, Sep. 2016, pp. 1–5.
[32] *Appl. Note 5SYA 2053-04*, ABB, Zürich, Switzerland, Sep. 2013.
[33] The Swedish Post and Telecom Authority. *Frequency Band for Block State*. Accessed: Jun. 20, 2021. [Online]. Available: https://www.pts.se/sv/bransch/radio/blocktillstand/
[34] K. Sharifabadi, L. Harnefors, H.-P. Nee, S. Norrga, and R. Teodorescu, "MMC-HVDC transmission technology and MTDC networks," in *Design, Control, Application Modular Multilevel Converters for HVDC Transmission Systems*. Chichester, U.K.: Wiley, 2016, pp. 336–372.
[35] T. Augustin, S. Norrga, and H.-P. Nee, "Modelling of HVDC breakers for HVDC grid simulations," in *13th IET Int. Conf. Power Transmiss.*, Manchester, U.K., 2017, pp. 1–6.
[36] R. P. P. Smeets and N. A. Belda, "High-voltage direct current fault current interruption: A technology review," *High Voltage*, vol. 6, no. 2, pp. 171–192, Apr. 2021. [Online]. Available: https://ietresearch.onlinelibrary.wiley.com/doi/abs/10.1049/hve2.12063
[37] T. Augustin, M. Becerra, and H.-P. Nee, "Enhanced active resonant DC circuit breakers based on discharge closing switches," *IEEE Trans. Power Del.*, vol. 36, no. 3, pp. 1735–1743, Jun. 2021.
[38] Edgewall Software. *802.11 Reference Design for WARP V3*. Accessed: Jun. 25, 2021. [Online]. Available: https://warpproject.org/trac/wiki/802.11
[39] *NR: Base Station (BS) Radio Transmission and Reception*, document 38.104, V17.3.0, 3rd Generation Partnership Project, Oct. 2021.

BARIŞ ÇIFTÇI (Graduate Student Member, IEEE) was born in Nazilli, Turkey, in 1987. He received the B.Sc. and M.Sc. degrees in electrical and electronics engineering from Middle East Technical University, Ankara, Turkey, and the Ph.D. degree in electrical engineering from the KTH Royal Institute of Technology, Stockholm, Sweden, in 2011, 2014, and 2022, respectively.

From 2011 to 2017, he was a Design Engineer and a Systems Engineer at Aselsan, Ankara, Turkey. He is currently a Development Engineer with Scania, Södertälje, Sweden. His research interest includes wireless control of modular multilevel converter submodules.

JAMES GROSS (Senior Member, IEEE) received the Ph.D. degree in telecommunications engineering from TU Berlin, Berlin, Germany, in 2006.

From 2008 to 2012, he was an Assistant Professor and a Research Associate at the Center of Excellence on Ultra-High Speed Mobile Information and Communication (UMIC), RWTH Aachen University, Aachen, Germany. Since November 2012, he has been a Professor of machine-to-machine communications with the School of Electrical Engineering and Computer Science, KTH Royal Institute of Technology, Stockholm, Sweden. From 2016 to 2019, he was the Director of the ACCESS Linnaeus Centre, KTH. He is currently an Associate Director of the newly formed KTH Digital Futures Research Center and the Co-Director of the newly formed VINNOVA Competence Center on Trustworthy Edge Computing Systems and Applications (TECoSA). He is the Co-Founder of R3 Communications GmbH—a Berlin-based venture capital-backed company in the area of ultra-reliable low-latency wireless networking for industrial automation. He has authored more than 150 peer-reviewed papers in international journals and conferences. His research interests include mobile systems and networks, critical machine-to-machine communications, edge computing, resource allocation, and performance evaluation. He was a recipient of multiple awards, including the Best Paper Awards at ACM MSWiM 2015, IEEE International Symposium on World of Wireless Mobile and Multimedia Networks (WoWMoM) 2009, and European Wireless 2009 and the ITG/KuVS Dissertation Award for his Ph.D. thesis, in 2007.

TIM AUGUSTIN was born in Berlin, Germany. He received the Diplom-Ingenieur degree in electrical engineering from the Dresden University of Technology, Germany, in 2015, and the Ph.D. degree from the KTH Royal Institute of Technology, Stockholm, Sweden, in 2021. He conducted research on dc circuit breakers at the KTH Royal Institute of Technology. His research interests include power electronics, switching devices, and electrical machines.

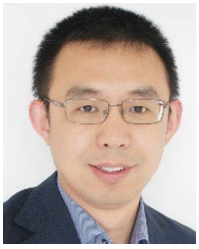

XIONGFEI WANG (Senior Member, IEEE) received the B.S. degree from Yanshan University, Qinhuangdao, China, in 2006, the M.S. degree from the Harbin Institute of Technology, Harbin, China, in 2008, both in electrical engineering, and the Ph.D. degree in energy technology from Aalborg University, Aalborg, Denmark, in 2013. Since 2009, he has been with the Department of Energy Technology, Aalborg University, where he became an Assistant Professor, in 2014, an Associate Professor, in 2016, a Professor and the Leader of Electronic Power Grid (eGRID) Research Group, in 2018. He has also been a Part-Time Professor with the KTH Royal Institute of Technology, Stockholm, Sweden, since 2020. His current research interests include modeling and control of power electronic converters and systems, stability and power quality of power-electronics-dominated power systems, and high-power converters.

Dr. Wang is a Member-at-Large of Administrative Committee for the IEEE Power Electronics Society (PELS) from 2020 to 2022. He was selected into the Aalborg University Strategic Talent Management Program, in 2016. He has received six Prize Paper Awards in the IEEE TRANSACTIONS and conferences, the 2018 Richard M. Bass Outstanding Young Power Electronics Engineer Award, the 2019 IEEE PELS Sustainable Energy Systems Technical Achievement Award, the 2020 IEEE Power & Energy Society Prize Paper Award, the 2020 JESTPE Star Associate Editor Award, and the Highly Cited Researcher in the Web of Science from 2019 to 2021. He is a Co-Editor-in-Chief of the IEEE TRANSACTIONS ON POWER ELECTRONICS LETTERS, and as an Associate Editor for the IEEE JOURNAL OF EMERGING AND SELECTED TOPICS IN POWER ELECTRONICS (JESTPE).

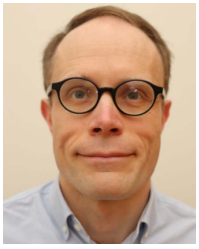

STAFFAN NORRGA (Member, IEEE) was born in Lidingö, Sweden, in 1968. He received the M.Sc. degree in applied physics from the Linköping Institute of Technology, Linköping, in 1993 and the Ph.D. degree in electrical engineering from the KTH Royal Institute of Technology, Stockholm, Sweden, in 2005.

From 1994 to 2011, he was a Development Engineer with ABB, Västerås, Sweden, in various power-electronics-related areas such as railway traction systems and converters for HVdc power transmission systems. He is currently an Associate Professor in power electronics with KTH. He is the Inventor or Co-Inventor of more than ten granted patents and has authored or coauthored more than 100 scientific papers published at international conferences or journals. His research interests include power electronics and its applications in power grids, renewables, and electric vehicles.

HANS-PETER NEE (Fellow, IEEE) was born in Västerås, Sweden, in 1963. He received the M.Sc., Licenciate, and Ph.D. degrees in electrical engineering from the KTH Royal Institute of Technology, Stockholm, Sweden, in 1987, 1992, and 1996, respectively. Since 1999, he has been a Professor of power electronics with the Department of Electrical Engineering, KTH Royal Institute of Technology. His research interests include power electronic converters, semiconductor components, and control aspects of utility applications, such as FACTS and high-voltage direct-current transmission, and variable-speed drives. Dr. Nee was a member of the Board of the IEEE Sweden Section for many years and was the Chair of the Board from 2002 to 2003. He is also a member of the European Power Electronics and Drives Association and is involved with its Executive Council and International Steering Committee.